Facile membrane preparation from colloidally stable metal-organic framework-polymer nanoparticles

Mingyuan Fang, J Cambedouzou, Didier Cot, Chaïmâa Gomri, Sabrina Nehache, Carmen Montoro, Mona Semsarilar

▶ **To cite this version:**

Mingyuan Fang, J Cambedouzou, Didier Cot, Chaïmâa Gomri, Sabrina Nehache, et al.. Facile membrane preparation from colloidally stable metal-organic framework-polymer nanoparticles. Journal of Membrane Science, 2022, 657, pp.120669. 10.1016/j.memsci.2022.120669 . hal-03729759

HAL Id: hal-03729759
https://hal.umontpellier.fr/hal-03729759

Submitted on 20 Jul 2022

HAL is a multi-disciplinary open access archive for the deposit and dissemination of scientific research documents, whether they are published or not. The documents may come from teaching and research institutions in France or abroad, or from public or private research centers.

L'archive ouverte pluridisciplinaire **HAL**, est destinée au dépôt et à la diffusion de documents scientifiques de niveau recherche, publiés ou non, émanant des établissements d'enseignement et de recherche français ou étrangers, des laboratoires publics ou privés.

Facile membrane preparation from colloidally stable Metal-Organic Framework-polymer nanoparticles

Received 00th January 20xx,
Accepted 00th January 20xx
Keywords: Metal-Organic Frameworks, polymers, membrane, RAFT, PISA, processability

Mingyuan Fang [a], Julien Cambedouzou [a], Didier Cot [a], Chaïmâa Gomri [a], Sabrina Nehache [a], Carmen Montoro,*[a,b] and Mona Semsarilar*[a]

[a.] *Institut Européen des Membranes—IEM UMR 5635, Univ Montpellier, CNRS, ENSCM, 34095 Montpellier, France.*
[b.] *Departamento de Química Inorgánica, Universidad Autónoma de Madrid, 28049 Madrid, Spain.*

UiO-MOFs are based on zirconium cluster and carboxylic acid linkers. They have excellent chemical and thermal stability, tolerance to linkers of different length and functionalities, making them good candidates for a broad range of applications. However, difficulties of processing the polycrystalline powder of MOFs limit their application. Here, we report for the first time the synthesis of the UiO-66 in the presence of a well-defined poly (methacrylic acid)-*b*-poly (methyl methacrylate) (PMAA-*b*-PMMA) nanoparticles (NPs) prepared *via* Reversible Addition–Fragmentation Chain-transfer Polymerization controlled Polymerization Induced Self-Assembly (RAFT-PISA). The PMAA-*b*-PMMA NPs with multi carboxylic acid groups on their surface, well defined in shape and size, act as multivalent connecting agent for the synthesis of the UiO-66. The resulting colloidally stable UiO-polymer NPs are crystalline, porous, and with an improved processability as was demonstrated by the preparation of a thin film nanocomposite (TFN) membrane. This membrane was applied in the filtration of Nickel(II) phthalocyanine-tetrasulfonic acid tetrasodium salt aqueous solution obtaining a water permeability *circa* 20 L m^{-2} h^{-1} bar^{-1} with a rejection of more than 90%. This unprecedented facile synthesis approach could be universally applied to other MOFs, expanding their application in different fields due to their enhanced processability.

1. Introduction

Metal Organic Frameworks (MOFs) are crystalline and porous materials constructed from the assembly of metal ions or clusters and organic linkers through coordination bonds.[1],[2] They show exceptional properties such as, high surface areas, high thermal and chemical stabilities, that make them useful in applications as varied as the capture and separation of gases,[3],[4],[5] catalysis,[6] drug delivery,[7] energy,[8],[9] sensing[10] and water treatment.[11],[12] Among numerous MOF structures reported, Zr-based MOFs have attracted considerable attention in recent years due to their exceptional stability in different solvents, like water, acetone and *N, N*-dimethylformamide (DMF).[13] In 2008, Lillerud *et al.*[14] reported the first example of such structure, UiO-66 (UiO from University of Oslo) based on Zr cluster and a dicarboxylate linker. Later, UiO-66 series have been obtained by varying the functionality as well as the length of the dicarboxylate linker.[15],[16] However, the crystalline nature of UiOs (and MOFs in general) limit their application in many fields since shaping and processing a polycrystalline powder is rather complicated. Various studies have focused on finding ways that facilitate MOF processing, mainly in the form of membranes[17] or thin films.[18],[19] One of the most used methods in the preparation of MOF membranes, consists of the dispersion of MOF within a polymeric matrix resulting in formation of mixed matrix membranes (MMMs).[20],[21] However, problems derived from particle agglomeration, weak interactions between MOF and the polymer matrix, results in membranes with non-uniform particle distribution and macro voids. To avoid particle-particle interactions causing particle agglomeration, Gascon *et al.*[22] recently demonstrated that surface modification of large ZIF-67 nanoparticles (NPs) using *N*-heterocyclic carbenes (NHCs), 1,3-bis(2,4,6-trimethylphenyl)imidazole-2-ylidene (IMes) and 1,3-bis(2,4,6-diisopropylphenyl)imidazole-2-ylidene (IDip) enhanced their processability in the liquid phase. The outer surface functionalization of ZIF-67 gave rise to MOF stable dispersions in non-polar solvents which could easily be blended with two polymer matrices (6FDA-DAM and 6FDA-DHTM-Durene) and form mixed matrix membranes. Alternative strategies are based on the surface

* E-mails: carmen.montoro@uam.es; mona.semsarilar@umontpellier.fr.
Electronic Supplementary Information (ESI) available: [DLS results, SAXS pattern, XRD patterns, FT-IR spectrum, TEM, SEM and optical images are included as Supporting Information.]. See DOI: 10.1039/x0xx00000x

functionalization of MOFs NPs by polymers to tune both their inter-particle interaction and their interaction with the polymer matrix which gives rise to stable suspensions with improved processability.[23],[24] In this sense, the bottom-up approach has also been employed to prepare colloidal dispersions of MOFs, where MOF synthesis is directly performed in the presence of polymers that act as soft templates or modulators. Lotsch *et al.*[25] used poly(acrylic acid) (PAA) and polyvinylpyrrolidone hexadecyltrimethylammonium bromide (PVP-CTAB) to fine tune the particle size of HKUST-1 and IRMOF-3 within a large range (30–300 nm). Thin films were prepared via spin-coating using this MOF colloidal solution. In a different study PAA was used to synthesize UiO-66, resulting in narrow particle size distributions with high colloidal stability.[26]

Apart from homopolymers, block copolymers have also been used in the synthesis of MOF structures (often as a soft template). Micelles formed from the self-assembly of amphiphilic block copolymers can act as surfactants, binding different functionalities with the metal clusters, stabilizing the forming MOF structure in solution and avoiding the phase separation of the formed crystalline structures via coordinating micelles.[27] Polystyrene-*b*-(acrylic acid) and polystyrene-*b*-polyvinylpyridine were used as templates for the preparation of ZIF-8 and HKUST-1.[28] The oligomers were assembled in solution forming spherical micelles and acted as preferential sites for the nucleation of MOF templating the crystal growth. Mesoporous HKUST-1 was also prepared in presence of poly(MAA-*b*-EDMA).[29] Likewise, triblock copolymers such as poly(ethylene oxide)-*b*-poly(propylene oxide)-*b*-poly-(ethylene oxide)s (PEO-*b*-PPO-*b*-PEO) has also been employed for the preparation of HKUST-1[30] and Ce-HMMOFs.[31]

In this article, we report for the first time the synthesis of UiO-66 (Scheme 1) in the presence of well-defined core cross-linked poly (methacrylic acid)-*b*-poly (methyl methacrylate) (PMAA-*b*-PMMA) NPs prepared *via* Reversible Addition−Fragmentation Chain-transfer Polymerization (RAFT) controlled by Polymerization Induced Self-Assembly (PISA).

Scheme 1. Proposed mechanism for the synthesis of UiO-66 initiated from the surface of (a) one core cross-linked PMAA-b-PMMA spherical NPs, (b) an agglomeration of more than one PMAA-b-PMMA

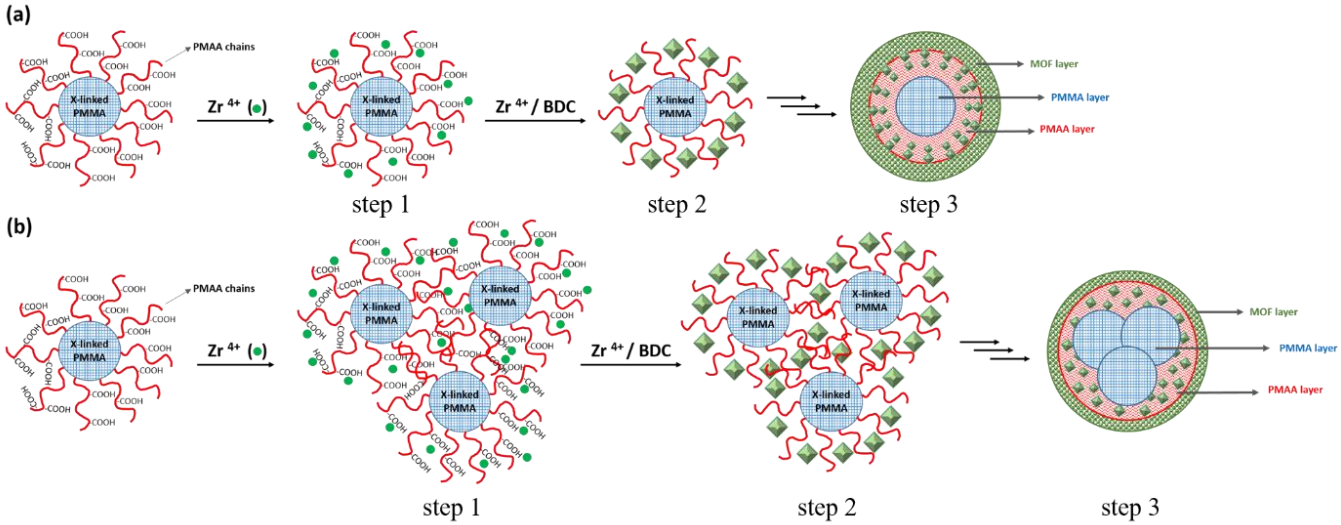

spherical NPs connected through Zr^{4+} ions, serving as preferential anchoring site for the growth of UiO-66.

These well-defined spherical NPs with multi carboxylic acid groups on their surface, stable in organic solvents, acted as nucleation sites for the synthesis of UiO-66. PISA has been developed for the facile synthesis of well-defined functional NPs with concentrations up to 50% w/w.[32] PISA formulations could be carried out in aqueous,[33] or organic solvents,[34] underlining the versatility of this approach. Here, an ethanolic PISA formulation was used to prepare the PMAA-*b*-PMMA spherical NPs with high surface area. The shape, colloidal stability and the surface functionality of the NPs were well preserved in different solvents (ethanol, water and DMF, please see Fig. S1) thanks to their cross-linked core. The carboxylic acid functionalities provided a strong interaction sites for the Zr ions/clusters. In addition, the presence of the flexible PMAA chains expanding through the UiO crystallites could link different MOF phases, resulting in formation of a

homogeneous, stable colloidal solution. This could simply be done by including the PMAA-*b*-PMMA NPs in the classical formulation of UiO-66 synthesis. Processability of the synthesized UiO-polymer NPs were tested *via* preparation of thin film nanocomposite (TFN) membrane by vacuum-assisted filtration of the UiO-polymer NPs on a nylon mechanical support. The prepared membrane was used in the removal of Nickel(II) phthalocyanine-tetrasulfonic acid tetrasodium salt from water.

2. Materials and methods

2.1. Materials

Methacrylic acid (MAA) (4-methoxyphenol, MEHQ used as inhibitor; 99.0%), 4-cyano-4-(phenylcarbonothioylthio) pentanoic acid (>97.0%), and 4,4-azobis(4-cyanovaleric acid) (ACVA; 98.0%), methyl methacrylate (MMA) (MEHQ used as inhibitor, 99.0%), 2,2'-azobis(2-methylpropionitrile) (AIBN; 98.0%), ethylene glycol dimethacrylate (EGDMA) (MEHQ used as inhibitor; 98%), (trimethylsilyl)diazomethane solution 2.0 M in diethyl ether, zirconium (IV) chloride ($ZrCl_4$; ≥99.5% trace metals basis), acetic acid (glacial, ≥99%) and nickel (II) phthalocyanine-tetrasulfonic acid tetrasodium salt were purchased from Sigma-Aldrich and terephthalic acid (≥98.0%), were purchased from Alpha Aesar. Solvents were purchased from Fisher Scientific and VWR. All the reagents were used without further purification. Nylon membrane was purchased from Filtres Fioroni, with an average pore size of 0.2 µm and a diameter of 47 mm.

2.2. Synthesis of poly(methacrylic acid) (PMAA)

PMAA macro chain transfer agent (mCTA) was synthesized based on our previously published work with some modifications.[35] MAA (12 g, 135.3 mmol), 4-cyano-4-(phenylcarbonothioylthio)pentanoic acid (540.8 mg, 1.93 mmol), and 4,4'-azobis (4-cyanovaleric acid) (54.26 mg, 0.19 mmol; CTA/ACVA molar ratio = 10) were dissolved in ethanol (12 g). The reaction mixture was sealed in a vessel and purged with nitrogen for 30 minutes and placed in a pre-heated oil bath at 70 °C for 6 h. The polymerization was quenched by cooling the reaction mixture to 20 °C and subsequently exposing the mixture to the air. The reaction mixture was diluted with a two-fold excess of ethanol. The unreacted monomer was removed by precipitation into a ten-fold excess of diethyl ether. The resulting solid was dried under vacuum for 24 h. ^{1}H NMR spectroscopy indicated a mean degree of polymerization (DP) of 64 for the PMAA macro-CTA, calculated by comparing the integrated signals due to the aromatic protons at 7.2–8.0 ppm with those due to the MAA backbone at 0.4–2.5 ppm.

2.3. Synthesis of poly(methacrylic acid)-b-poly(methyl methacrylate) diblock copolymer (PMAA-b-PMMA) NPs

(PMAA-*b*-PMMA) NPs were prepared *via* Reversible Addition−Fragmentation Chain-transfer Polymerization controlled Polymerization Induced Self-Assembly (RAFT-PISA). A typical ethanolic RAFT dispersion polymerization PMAA-*b*-PMMA synthesis at 20 wt% solids was adapted from our previously reported work. [35] MMA (0.9 g, 9 mmol), AIBN initiator (3.4 mg, 0.02 mmol), and $PMAA_{64}$ macro-CTA (380 mg, 0.07 mmol) were dissolved in ethanol (7 g). The reaction mixture was sealed in a 10 mL round bottom flask and purged with nitrogen for 10 min. The reaction flask was kept in a preheated oil bath at 70 °C for 24 h. ^{1}H NMR analysis indicated that MMA about 95% conversion was obtained after 26 h, a mean degree of polymerization (DP) of 124 was calculated. The PMAA-*b*-PMMA NPs were then cross-linked by addition of 10% of EGDMA and the reaction was carried out at 70°C for a further 12 h.

2.4. Synthesis of UiO-P-X% NPs

UiO-66 synthesis polymer-assisted was prepared by using four different concentrations of the core cross-linked PMAA-*b*-PMMA NPs in ethanol (10, 20, 40 and 80 % molar ratio of carboxylic acid function of PMAA-*b*-PMMA to zirconium; see details in Table S1). Briefly, $ZrCl_4$ (0.25 mmol, 58.3 mg) and terephthalic acid (0.25 mmol, 40.3 mg) were dissolved separately in 1.5 mL DMF. PMAA-*b*-PMMA NPs were dispersed in 1 mL of DMF and stirred for 1 hour. After that, this solution was mixed with the $ZrCl_4$ solution and then the terephthalic acid together with 0.5 mL of acetic acid (30 equivalent) were added. The final mixture was sonicated for 2 minutes and transferred to a 20 mL cylindrical glass pressure vessel that was heated at 120 °C. After 20 hours, a light pink colloidal or viscous solution of UiO-P-X% NPs in DMF was obtained, where X represents the molar percent of polymer NPs introduced into the synthesis. So, the samples were denoted as UiO-P-10%, -20%, -40% and -80%. To get the dry powder, the light pink suspension was centrifuged at 4.4 K rpm for 20 minutes and washed with 2 x 10 mL of

DMF and 3 x 10 mL of ethanol. Then, it was dried under vacuum at 80 °C for 8 hours.

2.5. Synthesis of UiO-66

UiO-66 was synthesized using the method previously reported by Behrens *et al.*[36] for 30 equivalent of acetic acid (see details in Table S1). After 20 hours of reaction at 120°C, white powder was obtained. The powder was centrifuged at 4.4k rpm for 5 minutes, washed with 2 x 10 mL of DMF and 3 x 10 mL of ethanol and finally dried under vacuum at 80 °C for 8 hours.

2.6. Kinetic study

Synthesis of UiO-66 in presence of 20 mol% of PMAA-*b*-PMMA NPs (UiO-P-20%) was followed at different intervals of time in order to establish the possible formation mechanism. Samples were taken at 0 min (T0min), 20 min (T20min), 40 min (T40min), 1 hour (T1h), 2 hours (T2h) and 20 hours (T20h). Thereafter, the evolution of particle size and crystallinity of the samples were monitored by SAXS and TEM analysis.

2.7. Preparation of the membranes

A TFN membrane was prepared by the 10 times dilution of 0.1 mL of UiO-P-20% colloidally stable solution in DMF and its deposition on a nylon membrane substrate using a vacuum-assisted filtration set-up. Then, the resulting TFN membrane was washed with 2 x 5 mL DMF and 3 x 5 mL ethanol. Finally, the membrane was dried under vacuum at 80 °C for 8 hours.
The control membrane preparation was carried out by depositing PMAA-*b*-PMMA solution on a nylon substrate membrane (about 5 µL of PMAA-*b*-PMMA ethanol solution diluted in 1 mL of DMF). The supported membrane was washed with 2 x 5 mL DMF, 3 x 5 mL EtOH and dried under vacuum at 80 °C for 8 hours.

2.8. Characterization

^{1}H NMR spectra were recorded at room temperature on a Bruker Advance spectrometer 400 MHz. Copolymer molecular weight distributions were determined using size exclusion chromatography (SEC) performed with a double detector array from Viscotek (TDA 305, Malvern Instruments, Worcestershire, UK). The Viscotek SEC apparatus was equipped with a two-column set-up with a common particle size of 5 mm using tetrahydrofuran (THF) as an eluent (1.0 mL min^{-1}). The Viscotek system contains a refractive index detector (RI, concentration detector). OmniSEC software was used for data analysis and acquisition. The number average molecular weights (Mn) and the dispersity index (Đ) were calculated relative to polystyrene standards. For SEC, the polymers were modified by methylation of the carboxylic acid groups on the PMAA block using an excess of trimethylsilyldiazomethane. Briefly, 20 mg of the polymer or copolymer were dissolved in THF and a yellow solution of trimethylsilyldiazomethane was added dropwise at room temperature. Upon addition, effervescence was observed, and the solution immediately became colorless. Addition of trimethylsilyldiazomethane was continued until the solution became yellow and effervescence ceased. Then, a small amount of trimethylsilyldiazomethane was added and the solution was stirred overnight. The centrifuges were performed through a Sigma Laboratory centrifuge. X-ray diffraction (XRD) was performed on a X'pert Pro (PAN Analytical). X-Ray diffractometer in reflectance parallel beam/parallel slit alignment geometry. The measurement employed Cu Kα line focused radiation at 800 W (40 kV, 20 mA) power. Samples were observed using a 0.017° 2θ step scan from 5° to 50° with an exposure time of 120 s per step. Small Angle X-ray Scattering (SAXS) analysis were performed in the transmission geometry of a laboratory set-up available at the Institut de Chimie Séparative de Marcoule. A GENIX Mo anode delivers an X-ray beam of wavelength 0.711 Å after crossing a XENOCS FOX2D monochromator. Collimation was achieved using two sets of FORVIS scatterless slits. Detection was made by a MAR345 imaging plate. Capillaries of diameter 2mm were used as sample holders. Absolute intensities were determined after proper calibration using a Good fellow polyethylene sample of width 2.36 mm and for which absolute intensity was equal to 4.9 cm^{-1} at scattering vector q = 0.37 nm^{-1}. SAXS profiles were simulated using the SASFit software.[37] Fourier-transform infrared (FT-IR) spectra were performed on a Thermo Nicolet iS50 FT-IR spectrometer in transmission mode. Membrane FT-IR spectra were performed on a Thermo Nicolet NEXUS FTIR spectrometer with a diamond ATR attachment. Thermogravimetric analysis (TGA) was measured by TA Instruments SDT Q600 by heating the sample to 1000 °C under nitrogen (100 mL min^{-1}) at a heating rate of 10 °C min^{-1}. Nitrogen adsorption isotherms were measured at 77 K on a Micromeritics ASAP 2020 Plus Adsorption Analyzer. Prior to measurement, powder samples were degassed for 12 h at 373 K. Dynamic light scattering (DLS) measurements were conducted on an Anton-

Paar Litesizer 500 at 20 °C. The DLS samples were diluted (50 folds) as compared to the original NP solutions. Scanning Electron Microscopy (SEM) images were observed under Hitachi S4800 with 0.1–30 kV working voltage. Membrane cross sections for SEM analysis were prepared in liquid nitrogen via freeze-fracturing. Transmission Electron Microscopy (TEM) images were obtained from JEOL 1200 EXII (or JEOL 1400 Flash) and JEOL 3000F under working voltages up to 120 kV and 300 kV, respectively. TEM samples were prepared using 10 µL of the sample placed on a carbon-coated copper grid for 60 s. The PMAA-*b*-PMMA samples were stained using ammonium molybdate for 20 s. Then the grid was dried using a vacuum hose under ambient conditions. All the image analysis were performed using ImageJ software. Optical microscope images were obtained by digital microscope Keyence VHX-7000.

2.9. Dye filtration experiment

The dye filtration experiment was carried out in a filtration cell (Amicon 8010, 10 mL filtration cell) which was connected to a water reservoir and a compressed air line. The effective area of the TFN membrane based on UiO-P-20% was 4.9 cm^2 and the feed volume was 10 mL. The membrane was firstly stabilized *via* filtration of deionized water with gradual increasing pressure from 0.5 to 2 bar for 2 hours and then kept the pressure at 2 bar for a further 2 hours. The excess of water was removed *via* dabbing with paper towel before performing the separation experiment. The experiment was performed at 0.5 bar using an aqueous solution of nickel (II) phthalocyanine-tetrasulfonic acid tetrasodium salt (~0.04 mM). Between different cycles of experiments, dye solution was charged back to the filtration cell and the membrane was not washed in order to avoid the dilution of the dye solution. The volumetric flux (J_v, L h^{-1} m^{-2}) and the permeability (L_P, L h^{-1} m^{-2} bar^{-1}) of the membrane were calculated according to Darcy's law using the following equations:

$$J_v = \frac{V_p}{t \cdot S} \quad (1)$$

$$L_P = \frac{J_V}{\Delta P} \quad (2)$$

where V_p represents the permeate volume (L), t is the time for permeate collection (h), S is membrane nanofiltration area (m^2) and ΔP is the pressure drop through the membrane (bar). The dye rejection was calculated by the equation:

$$D_{REJ}\ (\%) = [1 - \frac{C_p}{C_0}] \times 100 \quad (3)$$

where C_p and C_0 are the dye concentration in permeate and in feed solution, respectively. Both concentrations were determined by an UV spectrometer (SHIMADZU UV-2401PC spectrophotometer) at 625 nm that corresponds to the wavelength of maximum absorbance of nickel (II) phthalocyanine-tetrasulfonic acid tetrasodium salt.

3. Results and discussion

3.1. Characterization of the synthesized NPs

The spherical core cross-linked $PMAA_{64}$-*b*-$PMMA_{124}$ NPs were synthesized in alcohol *via* RAFT mediated PISA, following our previously reported procedure. [35],[38] In brief, a well-defined PMAA macro-CTA with a mean DP of 64 (*Mn*= 14.3 kg mol^{-1}, *Mw*= 14.9 kg mol^{-1}, *Đ*= 1.04) was block extended with MMA in ethanol under dispersion PISA conditions. The resulting $PMAA_{64}$–*b*-$PMMA_{124}$ (*Mn*= 18 kg mol^{-1}, *Đ*= 1.19) was core cross-linked *via* addition of EGDMA. The cross-linking of the core would prevent the NPs from solubilizing in organic solvents.

In order to have a larger surface area and more access to carboxylic functions on the surface of NPs, we chose to synthesize spherical PMAA-*b*-PMMA NPs (as compared to the other morphologies such as fibers and vesicles) that could provide more interactions with zirconium ions and Zr_6 clusters.

The morphology of PMAA-*b*-PMMA, UiO-P-X% NPs and UiO-66 MOF was analyzed by DLS, TEM and SEM (Table 1).

Table 1. NP size and particle morphology obtained using DLS, TEM and SEM.

Material	Size (nm) by DLS	Size (nm) by TEM	Size (nm) by SEM	Shape
PMAA-*b*-PMMA (Etanol)	37-44	23 ± 3	NA	Spherical
PMAA-*b*-PMMA (DMF)	27-56	34 ± 3	NA	Spherical
UiO-P-10%	170-240	144 ± 43	149 ± 24	Spherical

UiO-P-20%	170-220	130 ± 10	101 ± 18	Spherical
UiO-P-40%	175 - 265	65 - 210	70-200	Spherical
UiO-P-80%	128 - 228	50-110	57-160	Spherical
UiO-66	NA	500 ± 200	500 ± 200	octahedral

The hydrodynamic diameter of the PMAA-*b*-PMMA NPs in ethanol was 40 ± 4 nm (Fig. S1a), and 34 ± 12 nm in DMF (Fig. 1a). The size of the spherical NPs calculated using TEM images was 23 ± 3 nm in ethanol (Fig. S1b, S2a), and 34 ± 3 nm in DMF (Fig. 1d, S2b). The particles show similar hydrodynamic diameter in ethanol and DMF by DLS and dry state size (obtained from TEM image analysis). These data indicate the preservation of the spherical shape, size, and colloidal stability of the core cross-linked PMAA-*b*-PMMA NPs in both solvents. The size of the resulting UiO-P-X% NPs in DMF changed according to the quantity of PMAA-*b*-PMMA NPs introduced into the system.

When only 10% of polymer NPs was used, crystallites with average size from 170 to 240 nm were obtained (Fig. 1b). While when 20% of PMAA-*b*-PMMA was introduced in the system, particle size range was from 170 to 220 nm as judged by DLS measurements (Fig. 1c). When 40 mol % of polymer NPs were used, crystallites with size range from 175 to 265 nm (175 - 224 nm mainly) were obtained by DLS (Fig. S3a). While using 80 mol % of PMAA-*b*-PMMA NPs resulted in formation of particles with size of 128 - 228 nm (128-174 nm mainly) (Fig. S3b). The NPs observed by TEM showed a well-defined shape with a particle size of 144 ± 43 nm (Fig. 1e, S2c) for UiO-P-10% and 130 ± 10 nm (Fig. 1f, S2d) for UiO-P-20%. In case of UiO-P-20%, no precipitation was observed after being left unstirred for a month at ambient conditions (Fig. S4). It seems that by increasing the quantity of PMAA-*b*-PMMA NPs to 20 mol %, a good control over the homogeneity and colloidal stability could be reached. In contrast, when the amount of PMAA-*b*-PMMA NPs were increased, the crystallites of UiO-P-40% observed by TEM showed a non-regular spherical shape with particle size of 65 to 210 nm (Fig. S3c) with 2 main populations (100 to 160nm and 160 to 200 nm). It is more difficult to observe individual crystallites in the UiO-P-80% sample as the solution was very viscous (gel-like) and difficult to re-disperse. The size of these particles ranged between 50 to 110 nm. To confirm that the stability of the hybrid particles was due to the direct growth of the UiO-66 structure within the hairy shell formed by PMAA chains, a mixture of pristine UiO-66 powders with the 20 mol % of PMAA-*b*-PMMA NPs was prepared in DMF (see supporting information for full details). This mixture was colloidally unstable and phase separated rather rapidly after stopping the stirring (Fig. S5). It could clearly be observed that the growing of UiO-66 from the surface of the PMAA-*b*-PMMA NPs totally changed the hydrodynamic properties of the UiO-P-X% NPs as compared to the core cross-linked polymer NPs. The shape of the UiO-P-X% NPs were no longer perfectly spherical as the edges started becoming angular and sharp (Fig. 1). UiO-P-X% powder isolated from the suspension were also imaged using SEM and TEM and compared to pristine UiO-66 (Fig. S6). Under SEM the pristine UiO-66 showed polydisperse crystals with octahedral shape with size range of 300 to 700 nm (Fig. S6a). Similar particles size could also be observed under TEM with cubic shape showed on two-dimensional TEM image (Fig. S6b). Shape and size of the dry UiO-P-X% NPs were comparable to what was observed for UiO-P-X% NPs in its original state in DMF. UiO-P-10% and UiO-P-20% crystallite size were 149 ± 24 nm and 101 ± 18 nm respectively (Fig. S6c, S6d). UiO-P-40% presented a spherical shape with sharp edges, with size range

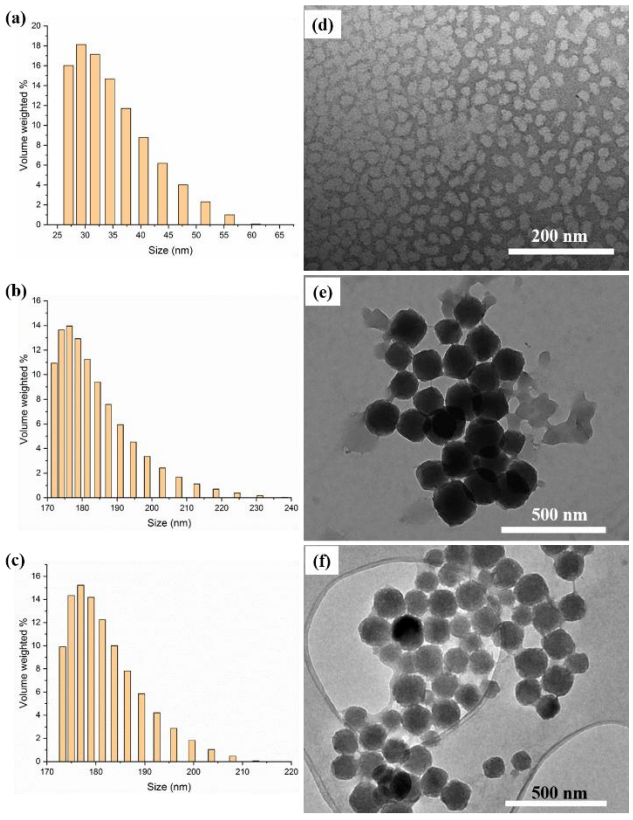

of 70-200 nm (Fig. S7a, S7b). Shape and size of UiO-P-X% crystallites could not be observed well under SEM, especially for the UiO-P-80%, since the MOF portion of the sample was rather little. Under SEM the UiO-P-80% (Fig. S7c, S7d) seems like a

Structural characterization of UiO-P-X% was carried out by XRD measurements. The diffraction patterns (Fig. 2) show the major peaks of pristine UiO-66 confirming the formation of the same crystalline structure. This means that the presence of PMAA-*b*-PMMA NPs does not affect the crystalline phase growth of the UiO-66. However, the intensity of the main signals decreased, and peaks became wider with the increasing amount of the amorphous polymer NPs.

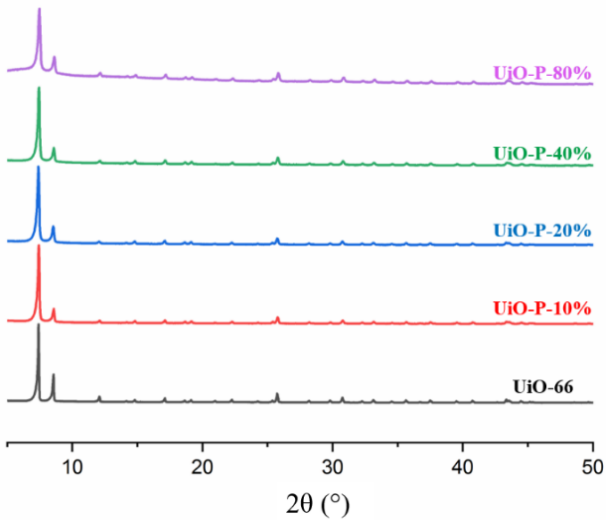

Fig. 2. XRD patterns of pristine UiO-66, UiO-P-10%, UiO-P-20%, UiO-P-40% and UiO-P-80%.

The chemical composition of the hybrid UiO-P-X% NPs was analyzed by FT-IR measurements (Fig. 3). It was noted that the characteristic C=O stretching of the uncoordinated carboxylate group at 1730 cm^{-1} and C-H stretching of methyl and methylene groups between 2995 and 2955 cm^{-1} from PMAA-*b*-PMMA NPs appeared in UiO-P-X% samples and the intensity of the bands increased with the increasing amount of the polymer NPs. The two intense bands around 1590 cm^{-1} and 1401 cm^{-1} are assigned to the asymmetric and symmetric stretch vibrations of C=O group, respectively, in the coordinated carboxylate group. Moreover, the band around 550 cm^{-1} represents the Zr–(O=C) asymmetric stretch. [39], [40] These results indicate that PMAA-*b*-PMMA NPs are participating in the interaction with the metal clusters during the UiO-66 crystallites formation. The presence of PMAA-*b*-PMMA NPs in the synthesized materials was also corroborated by TGA (Fig. 4). The TGA profiles show that UiO-P-X% NPs go through a multistep gradual decomposition continues polymer film with embedded UiO particles (size from 57 to 160 nm).

Fig. 1. Particle size distribution obtained from DLS for (a) PMAA-*b*-PMMA, (b) UiO-P-10% (c) UiO-P-20% in DMF and TEM images for (d) PMAA-*b*-PMMA, (e) UiO-P-10% and (f) UiO-P-20% in DMF. while pristine UiO-66 decomposed in three main steps. This difference is due to the presence of PMAA-*b*-PMMA NPs coordinated to UiO-66 NPs which decomposed in two steps. However, it is difficult to determinate the exact amount of incorporated PMAA-*b*-PMMA NPs since the organic linker decomposition of UiO-66 also takes place at the same temperature range (between 300 and 500 ºC). If the initial weight loss (due to free water loss below 100°C) is not accounted for, the weight loss of UiO-P-10% and UiO-P-20% at 800 °C is 5-7% higher than the pristine UiO-66. However, the additional weight loss at 800 °C for UiO-P-40% and UiO-P-80% were 17.6% and 24.7% higher than UiO-66 respectively.

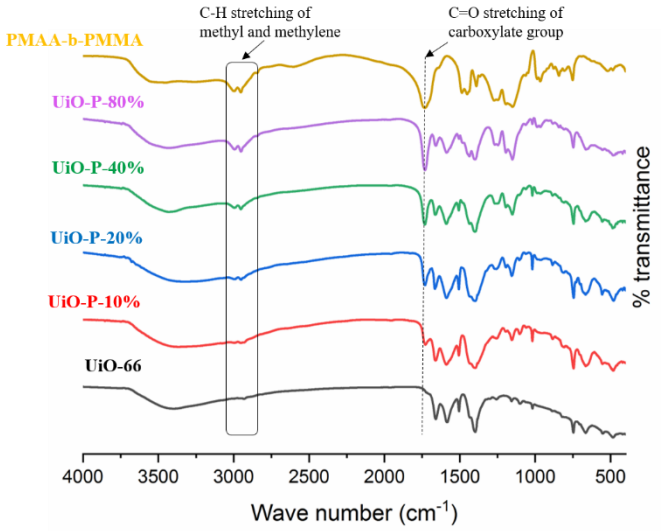

Fig. 3. FT-IR spectrum for UiO-66, UiO-P-10%, UiO-P-20%, UiO-P-40%, UiO-P-80% and PMAA-b-PMMA NPs.

The additional weight loss could also be an indication of the copolymer fraction incorporated in the hybrid structure (weight percentage of the PMAA-*b*-PMMA NPs present in the UiO-polymer hybrid structure). Moreover, it should be pointed out that incorporation of low amounts of polymer

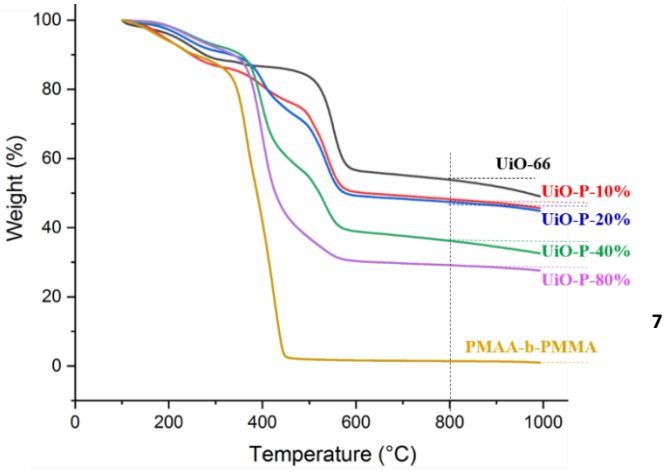

NPs in the MOF structure (UiO-P-10% and UiO-P-20%) has a low impact on the thermal stability of the UiO-66.

Fig. 4. TGA thermograms for pristine UiO-66, UiO-P-10%, UiO-P-20%, UiO-P-40%, UiO-P-80% and PMAA-*b*-PMMA NPs.

The nitrogen adsorption isotherms (Fig. 5) of the pristine UiO-66, exhibit a typical type I isotherm at 77K with a Brunauer–Emmett–Teller (BET) surface area of 1136 $m^2\ g^{-1}$ indicating the uniform microporous structure of UiO-66. UiO-P-10% and UiO-P-20% showed BET surface areas of 758 and 812 $m^2\ g^{-1}$, respectively. As it was expected, the adsorption capacity decreased around 30 % with the decreasing size of the NP. This also highlights that the presence of the polymer NPs does not affect the accessibility of majority of the micropores in the MOF-polymer structure.

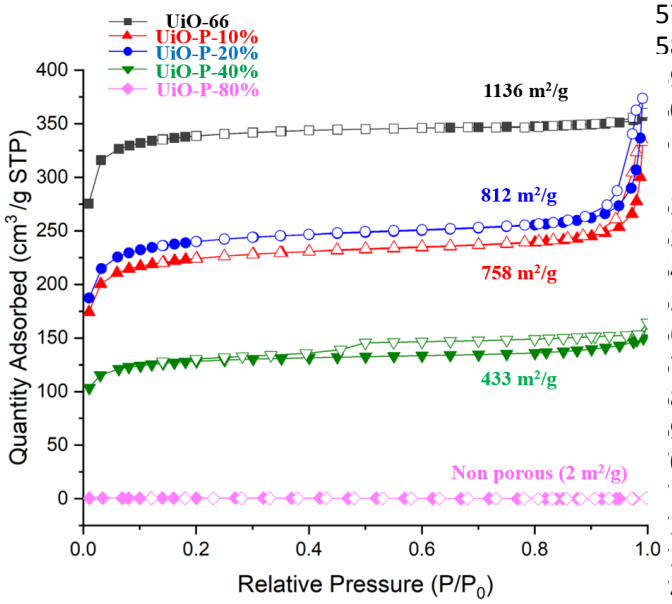

Fig. 5. N_2 adsorption isotherms measured at 77 K for pristine UiO-66, UiO-P-10%, UiO-P-20%, UiO-P-40% and UiO-P-80%. Filled and empty symbols represent adsorption and desorption, respectively.

However, the introduction of higher amounts of the non-porous polymer NPs has decreased the surface area, UiO-P-40% exhibit surface areas of 433 $m^2\ g^{-1}$ (about 38% of surface area compared to pristine UiO-66). Then, when the PMAA-*b*-PMMA NPs content reach to 80 mol %, the obtained hybrid became nonporous with a BET surface area of only 2 m^2/g. PMAA-*b*-PMMA NPs would become rigid and lose their flexibility under such low temperature. It is possible that the UiO-polymer hybrid could show better pore accessibility in solution. However, to confirm this a complete study needs to be carried out. The UiO-P-10%, UiO-P-20% and UiO-P-40% isotherms showed hysteresis loops in the high relative pressure region, may indicate the appearance of mesopores by introducing the PMAA-*b*-PMMA NPs. The BJH desorption pore analysis (Fig. S10a and S10b) of UiO-P-10%, UiO-P-20% and UiO-P-40% showed small mesopores within the range between 3 and 4 nm. The UiO-P-10% and UiO-P-20% also presented large mesopores from 10 to 50 nm. One hypothesis about the source of large mesopores is that initial space occupied by the swollen polymer particles in DMF was partially released, because of the collapse of polymer particles during the drying and analysis under low temperature (Fig. S10c). More careful analysis is needed to investigate this effect. These results show that for having a performant MOF material the removal of the polymer particles is not necessary as the performance of resulting unprecedented UiO-polymer NPs are comparable to the pristine UiO-66 while showing immense improvement in terms of processability as it will be demonstrated below.

3.2. Kinetic study

With the aim to understand how the UiO-66 was formed in the presence of PMAA-*b*-PMMA NPs, a kinetic study was performed, monitoring the evolution of particle size and crystallinity by SAXS and TEM.

The SAXS profile of PMAA-*b*-PMMA NPs dispersed in DMF is shown in Fig. S8. At lower angles, the intensity decrease shows no specific feature until the appearance of two oscillations with intensity maxima located at scattering vector q = 0.4 and 0.6 nm^{-1} (Fig. S8a, S8b), respectively. Such oscillations could be related to the form factor of dispersed nanometric objects of size larger than 14 nm, whose lower angle signature involving the intensity plateau and the first oscillations are hidden by a more intense signal coming from other objects in the sample (e.g., particle substructure such as pores). Fig. S8c shows a simulation of the SAXS intensity originating from monodisperse spherical particles with diameter of 34 nm (obtained using the SASFit software). It can be seen that the two oscillations seen on the experimental pattern match the fourth and combination of fifth and sixth oscillations of the form factor of such objects, which are of similar size obtained from TEM and DLS.

Given the fast kinetics of the reaction, it was not possible to perform an in-situ SAXS experiment. Instead, samples at different time intervals were taken during the reaction. The SAXS pattern of the reaction mixture containing all the precursors for synthesis of UiO-P-20% (T0) shows two peaks at scattering vectors q of 5.27 and 6.10 nm^{-1} (Fig. 6a).

These two peaks correspond to the first two peaks of the typical UiO-66, indicating that there was already a small amount of UiO-polymer hybrid present in the reaction mixture. TEM analysis showed no large particles or crystals at this early stage (Fig. 6d). At 20 minutes, the reaction mixture started to turn opaque (as compared to transparent) and the two peaks at q = 5.27 and 6.10 nm^{-1} became more intense. In addition, a new signal at q = 8.61 nm^{-1} appeared in the pattern (Fig. 6a). These observations indicate the continuous growth of UiO-polymer hybrid crystals as a function of time. Similar trend could be observed in TEM images, where a large number of small crystals with size between 25 to 60 nm were visible (Fig. 6e).

At 40 min, the reaction medium turned milky white. SAXS pattern showed more intense signals with two new peaks at q = 10.55 and 15.87 nm^{-1} that could highlight the enhancement of crystallinity and continuous growth of the UiO-66 crystals on the block copolymer NPs. TEM images also showed the growth of UiO-P-X%. The size of the crystals was 80-120 nm with spherical morphology (Fig. S9a).

Similar trend could be observed for samples taken between 1 to 20 hours (T1h and T20h). SAXS patterns showed more and more intense peaks, referring to the enhancement of crystallinity (Fig. 6a). TEM images revealed spheres with narrow distribution as a function of the reaction time (Fig. S9b-c and Fig. 6f).

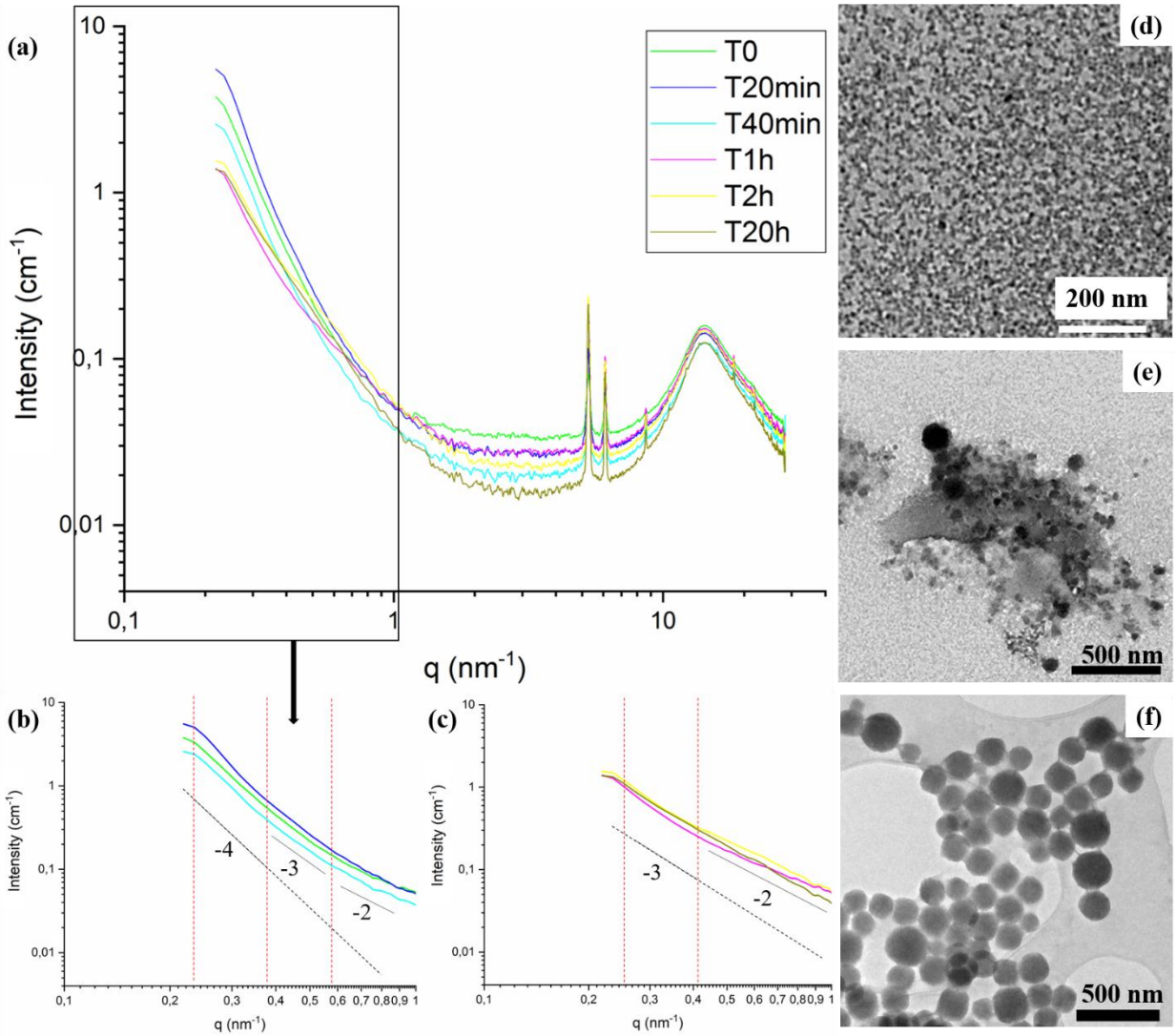

Fig. 6. (a) SAXS pattern of UiO-P-20% T0min to T20h, (b-c) magnification of the SAXS patterns in the small angles region and the power laws of intensity in the region; TEM images for (d) T0, (e) T20min and (f) T20h.

An important point to be noted in the SAXS patterns, is the slope of the linear regions between q = 0.25 to 0.4 nm^{-1}, 0.4 to 0.6 nm^{-1} and 0.6-1 nm^{-1}. These correspond to power laws in such log-log

representations of the SAXS patterns. They changed significantly after 1 hour of reaction (Fig. 6b-c, Table S2). The power laws of the intensity decrease before 1 hour (T0, T20min and T40min samples) are respectively -4 from q = 0.25 to 0.5 nm^{-1}, –3 from q = 0.4 to 0.6 nm^{-1}, and -2 from q = 0.6 to 1 nm^{-1} (Fig. 6b). Two inflexions could be found at q = 0.4 and 0.6 nm^{-1}, representing the distances of ~16 nm and ~10 nm. After 1 hour of reaction, the power laws of intensity in the region where q ranges from 0.25 to 0.4 nm^{-1} decreased to –3 (T1h, T2h and T20h). The change of power laws in this region from -4 to -3 may indicate the increasing of particle size of UiO-polymer hybrids. This means that the -4-power law domain has been shifted to the lower angles which is not reachable with the used experiment set-up. Moreover, for q values ranging from 0.4 to 1 nm^{-1}, the power laws decrease to –2 and the second inflexion point is lost (Fig. 6c).

The power law decrease at smaller angles (-4 to -3) may correspond to the increase of the largest particles roughness. In the q range between 0.4 and 0.6 nm^{-1}, it is not easy to explain the change of intensity power law from -3 to -2 in terms of morphological changes. The evolution of the overall shape of the SAXS profile in this mid -q range could also be attributed to an increase of intensity related to typical distances of 10-16 nm. Such a signal could originate from the emergence of a porous organization at 10 nm scale, which also affects the surface of NPs by increasing their roughness (Fig. 6f, S9d). The power laws in the range where q is larger than 0.6 nm^{-1} are not relevant as intensity is low and might be impacted by smaller intermolecular distances in the sample.

3.3. Proposed formation mechanism and structure

Based on the previous results two formation routes could be proposed (Scheme 1). The addition of the acid decorated polymer NPs to the synthesis of UiO-66 would result in the chelation of the zirconium ions and clusters to the poly (methacrylic acid) chains forming the shell of the polymer NPs (step 1). From this point on the synthesis of the UiO-66 would be carried out as in the case of classical UiO-66 (steps 2 and 3). This route should result in the formation of much smaller hybrid UiO-polymer NPs as the initial size of the PMAA-PMMA NPs were about 34 nm. The size of the hybrid NPs calculated from the TEM images is 130-140 nm (4 times bigger than the polymer NPs). This would mean that the UiO-66 would start growing within the hairy PMAA chains, growing outwards, until complete covering of the polymer NPs. Complete coverage of the PMAA shell, should result in the loss of colloidal stability of the hybrid NPs, which is not the case here. The hybrid NPs synthesized showed high colloidal stability over a long period. This suggests that the second pathway would be more probable. In the pathway depicted in Scheme 1b, the preferential adsorption of the Zr ions to the acid groups on the surface of the particles would link two or more polymer NPs together (step 1) where then the UiO-66 network would start forming (step 2 and 3). The coagulation of few polymer NPs would mean that less acid groups would be engaged in the MOF formation (hence more free acid groups). These results in formation of a less dense layer of UiO-66, more free acid groups penetrated through the thin layer of UiO-66 that could explain the observed UiO-P-X% particle size and their prolonged colloidal stability.

3.4. Characterization of the membranes

Majority of MOF based-membranes are in the form of MMMs. In such membranes, the MOF crystals are dispersed in a polymer solution matrix prior to casting. Although, extensively synthesized as used specifically for gas separation, their weakness lies in the fact that the two mixed materials (MOF and polymer) are incompatible. This chemical incompatibility results in inhomogeneous distribution of the MOF fillers in the polymer matrix. To date several different approaches have been employed to homogeneously distribute the MOF.[22],[25],[26]

The optimal properties of the UiO-P-20% NP suspension in terms of particles size homogeneity and colloidal stability, made it ideal for the preparation of a TFN membrane which showed good mechanical properties such as stability and flexibility (Fig. 7a). The XRD (Fig. S11) and FT-IR (Fig. S12) measurements showed that the crystallinity and chemical functionalities of UiO-P-20% were maintained during membrane preparation. The TFN membrane was then observed under optical microscope (Fig. 7b) to ensure the full coverage and fissure free layer of UiO-P-20% on the nylon support. In addition, the membranes analysis using SEM revealed a continuous layer and homogeneous MOF-polymer NP distribution on the surface of the membrane (Fig. 7c).

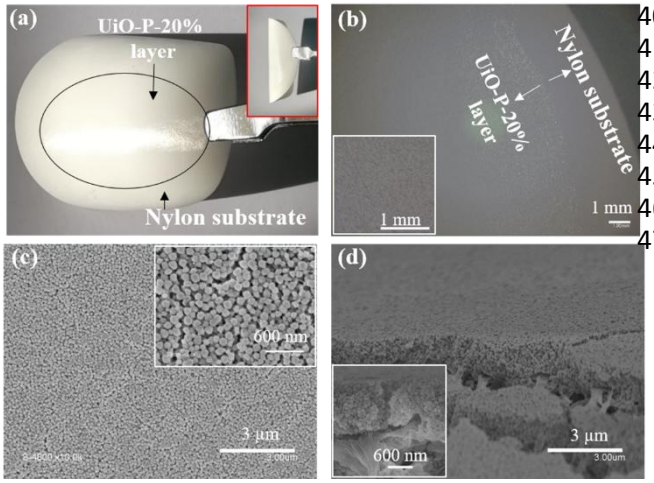

Fig. 7. UiO-P-20% nylon supported membrane images (a) optical, (b) optical microscope, and SEM (c) top view, (d) cross-section.

The cross-section SEM images of the membrane showed a compact thin film layer of UiO-P-20% NPs (Fig. 7d, Fig. S13) with an average thickness of 1 µm. For comparison, a control membrane was also prepared using a mixture of pristine UiO-66 powder and PMAA-*b*-PMMA NPs dispersed in DMF (Fig. S14). This membrane showed different aspect compared to UiO-P-20% nylon supported membrane. From the top view under SEM (Fig. S15 a-b), the membrane showed a non-continuous layer with numerous uncovered areas where the nylon support could be detected directly (inhomogeneous coverage with thickness from 0.8 to 3 µm).

3.5. Dye filtration experiment results

Membrane filtration properties were studied by the filtration of an aqueous solution of nickel (II) phthalocyanine-tetrasulfonic acid tetrasodium salt as guest molecule through the TFN membrane based on UiO-P-20%. The results showed that more than 90% of the dye was rejected (Fig. 8) from the solution compared to less than 9% of dye rejection by using the PMAA-*b*-PMMA membrane (Fig. S15) after 7 filtration cycles. In contrast, the average water permeability of the TFN membrane based on UiO-P-20% was around 20.4 L m^{-2} h^{-1} bar^{-1} for the first 5 cycles (Fig. S16) which is largely less as compared to 410 L m^{-2} h^{-1} bar^{-1} of PMAA-*b*-PMMA membrane. This decrease in the permeability is clearly due to the presence of the UiO-66 structure with a different pore size as compared to those in the membrane prepared from block copolymer NPs. Through further image treatment, (distance map of binary images and manual measurement; see Fig. S17, S18; Table S3) and comparison of membrane permeability [35], an inter particle distance of approximately 12.4 nm could be estimated. The membranes were characterized after dye filtration using XRD (Fig. S11) and FT-IR (Fig. S12) to confirm the membrane stability. The results suggested that both crystallinity and integrity of the TFN membrane based on UiO-P-20% were perfectly maintained after the filtration process.

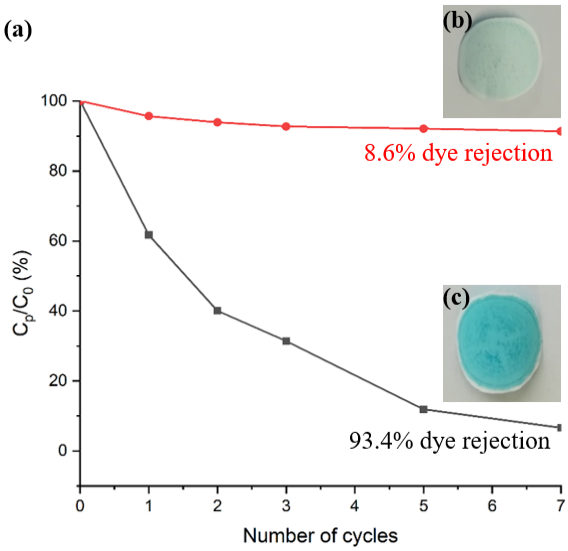

Fig. 8. (a) Dye concentration evaluation at different cycles, PMAA-*b*-PMMA membrane, UiO-P-20% membrane; Optical image of the nylon supported membranes after dye filtration (b) PMAA-*b*-PMMA (c) UiO-P-20% membranes.

4. Conclusions

A novel pathway for the synthesis of UiO-66 was carried out in the presence of well-defined spherical PMAA-*b*-PMMA NPs. Some of the resulting crystalline hybrid NPs were monodisperse and showed long-term colloidal stability. The core cross-linked spherical PMAA-*b*-PMMA NPs used in the presented approach is advantageous as a major challenge in the use of self-assembled surfactants and block copolymers in the synthesis of MOFs is the obligation to perform the synthesis in aqueous or alcohol media since the self-assembled structures would dissociate in organic solvents. However, majority of MOFs are synthesized in organic solvents such as DMF. The characterization of the resulting UiO-P-X% NPs both at colloidal and solid state indicated that they have comparable properties in terms of crystallinity, thermal stability, and porosity to the pristine UiO-66. This simple approach only requires the addition of the PMAA-*b*-PMMA NPs to the classical UiO-66 synthesis formulation and does not need any special treatment including the removal of PMAA-

b-PMMA NPs as often is the case when polymers are used.[28] The incorporation of the diblock copolymer NPs in the MOF structure renders high colloidal stability and flexibility to the UiO-66 structure while maintaining the fundamental MOF properties such as crystallinity and porosity. Moreover, straightforward approach could be easily applied for the synthesis of other carboxylic acid-based MOFs with enhanced processability unknown to MOFs, which would lead to their use in numerous different applications since they could be shaped and processed easily. To demonstrate their processability a TFN membrane based on UiO-P-20% NPs was prepared. Unlike other reported membranes based on UiO or other families of MOFs, the presented method here does not require time-consuming mixing process with a polymer matrix nor chemical modification of the matrix. The membrane properties and separation capacity were verified using a model dye compound. The results suggested that the UiO-polymer selective layer, could reach rejection values of more than 93%. This approach offers a simple and highly adaptable pathway to make robust membranes using different substrates suitable for a wide range of application.

Author Contributions

The manuscript was written through contributions of all authors. All authors have given approval to the final version of the manuscript.

Conflicts of interest

There are no conflicts to declare.

Acknowledgements

Mathias Gravelle is thanked for his help with experimental setups. MF acknowledges the financial support of China Scholarship Council (CSC), grant number 201708070001. INC-CNRS is thanked for the post-doctoral fellowship of CM. CM also acknowledges the financial support of Madrid Government under the Multiannual Agreement with Universidad Autónoma de Madrid in the context of the V PRICIT. (SI1/PJI/2019-00505). Institut Carnot is also acknowledged for supporting this project.

References

[1] H.-C. Zhou, J. R. Long, O. M. Yaghi, *Chem. Rev.* **2012**, *112*, 673.

[2] N. Stock, S. Biswas, *Chem. Rev.* **2012**, *112*, 933.

[3] L. J. Murray, M. Dinca, J. R. Long, *Chem. Soc. Rev.* **2009**, *38*, 1294.

[4] E. Barea, C. Montoro, J. A. R. Navarro, *Chem. Soc. Rev.* **2014**, *43*, 5419.

[5] V. Colombo, C. Montoro, A. Maspero, G. Palmisano, N. Masciocchi, S. Galli, E. Barea, J. A. R. Navarro, *J. Am. Chem. Soc.* **2012**, *134*, 12830.

[6] A. Corma, H. Garcia, F. X. Llabres i Xamena, *Chem. Rev.* **2010**, *110*, 4606.

[7] P. Horcajada, C. Serre, G. Maurin, N. A. Ramsahye, F. Balas, M. Vallet-Regí, M. Sebban, F. Taulelle, G. Férey, *J. Am. Chem. Soc.* **2008**, *130*, 6774.

[8] P. Ramaswamy, N. E. Wong, G. K. H. Shimizu, *Chem. Soc. Rev.* **2014**, *43*, 5913.

[9] C. Montoro, P. Ocón, F. Zamora, J. A. R. Navarro, *Chem. - A Eur. J.* **2016**, *22*, 1646.

[10] L. E. Kreno, K. Leong, O. K. Farha, M. Allendorf, R. P. Van Duyne, J. T. Hupp, *Chem. Rev*, **2012**, 112, 1105.

[11] C. Wang, X. Liu, N. K. Demir, J. P. Chen, K. Li, *Chem. Soc. Rev.* **2016**, *45*, 5107.

[12] M. S. Denny, J. C. Moreton, L. Benz, S. M. Cohen, *Nat. Rev. Mater.* **2016**, *1*, 16078.

[13] Y. Bai, Y. Dou, L. H. Xie, W. Rutledge, J. R. Li, H. C. Zhou, *Chem. Soc. Rev.* **2016**, *45*, 2327.

[14] J. H. Cavka, S. Jakobsen, U. Olsbye, N. Guillou, C. Lamberti, S. Bordiga, K. P. Lillerud, *J. Am. Chem. Soc.* **2008**, *130*, 13850.

[15] S. J. Garibay, S. M. Cohen, *Chem. Commun.* **2010**, *46*, 7700.

[16] J. Ru, X. Wang, F. Wang, X. Cui, X. Du, X. Lu, *Ecotoxicol. Environ. Saf.* **2021**, *208*, 111577.

[17] X. Li, Y. Liu, J. Wang, J. Gascon, J. Li, B. Van Der Bruggen, *Chem. Soc. Rev.* **2017**, *46*, 7124.

[18] Z. Liao, T. Xia, E. Yu, Y. Cui, *Crystals* **2018**, *8*, 338.

[19] D. Zacher, O. Shekhah, C. Wöll, R. A. Fischer, *Chem. Soc. Rev.* **2009**, *38*, 1418.

[20] L. Paseta, D. Antorán, J. Coronas, C. Téllez, *Ind. Eng. Chem. Res.* **2019**, *58*, 4222.

[21] B. Seoane, J. Coronas, I. Gascon, M. E. Benavides, O. Karvan, J. Caro, F. Kapteijn, J. Gascon, *Chem. Soc. Rev.* **2015**, *44*, 2421.

[22] A. Knebel, A. Bavykina, S. J. Datta, L. Sundermann, L. Garzon-Tovar, Y. Lebedev, S. Durini, R. Ahmad, S. M. Kozlov, G. Shterk, M. Karunakaran, I. D. Carja, D. Simic, I. Weilert, M. Klüppel, U. Giese, L. Cavallo, M. Rueping, M. Eddaoudi, J. Caro, J. Gascon, *Nat. Mater.* **2020**, *19*, 1346.

[23] M. Kalaj, K. C. Bentz, S. Ayala, J. M. Palomba, K. S. Barcus, Y. Katayama, S. M. Cohen, *Chem. Rev.* **2020**, *120*, 8267.

[24] F. Jin, J. Liu, Y. Chen, Z. Zhang, *Angew. Chemie - Int. Ed.* **2020**, 60, 14222.
[25] A. Ranft, S. B. Betzler, F. Haase, B. V. Lotsch, *CrystEngComm* **2013**, *15*, 9296.
[26] K. C. Bentz, S. Ayala, M. Kalaj, S. M. Cohen, *Aust. J. Chem.* **2019**, *72*, 848.
[27] M. L. Hu, M. Y. Masoomi, A. Morsali, *Coord. Chem. Rev.* **2019**, *387*, 415.
[28] S. Cao, G. Gody, W. Zhao, S. Perrier, X. Peng, C. Ducati, D. Zhao, A. K. Cheetham, *Chem. Sci.* **2013**, *4*, 3573.
[29] H. Martínez-Pérez-Cejuela, M. Guiñez, E. F. Simó-Alfonso, P. Amorós, J. El Haskouri, J. M. Herrero-Martínez, *Microchim. Acta* **2020**, *187*, 1.
[30] M. H. Pham, G. T. Vuong, F. G. Fontaine, T. O. Do, *Cryst. Growth Des.* **2012**, *12*, 1008.
[31] K. Li, J. Yang, R. Huang, S. Lin, J. Gu, *Angew. Chemie* **2020**, *132*, 14228.
[32] N. J. W. Penfold, J. Yeow, C. Boyer, S. P. Armes, *ACS Macro Lett.* **2019**, *8*, 1029.
[33] N. J. Warren, S. P. Armes, *J. Am. Chem. Soc.* **2014**, *136*, 10174.
[34] M. J. Derry, L. A. Fielding, S. P. Armes, *Prog. Polym. Sci.* **2016**, *52*, 1.
[35] L. Upadhyaya, M. Semsarilar, R. Fernández-Pacheco, G. Martinez, R. Mallada, A. Deratani, D. Quemener, *Polym. Chem.* **2016**, *7*, 1899.
[36] A. Schaate, P. Roy, A. Godt, J. Lippke, F. Waltz, M. Wiebcke, P. Behrens, *Chem. - A Eur. J.* **2011**, *17*, 6643
[37] I. Breßler, J. Kohlbrecher, A. F. Thünemann, *J. Appl. Crystallogr.* **2015**, *48*, 1587.
[38] L. Upadhyaya, M. Semsarilar, S. Nehache, D. Cot, R. Fernández-Pacheco, G. Martinez, R. Mallada, A. Deratani, D. Quemener, *Macromolecules* **2016**, *49*, 7908.
[39] L. Valenzano, B. Civalleri, S. Chavan, S. Bordiga, M. H. Nilsen, S. Jakobsen, K. P. Lillerud, C. Lamberti, *Chem. Mater.* **2011**, *23*, 1700.
[40] S. Chavan, J. G. Vitillo, D. Gianolio, O. Zavorotynska, B. Civalleri, S. Jakobsen, M. H. Nilsen, L. Valenzano, C. Lamberti, K. P. Lillerud, S. Bordiga, *Phys. Chem. Chem. Phys.* **2012**, *14*, 1614.